Particle dispersion in porous media: Differentiating effects of geometry and fluid rheology

Jack D. C. Jacob,[1] Ramanan Krishnamoorti,[1,2,*] and Jacinta C. Conrad[1,†]
[1]*Department of Chemical & Biomolecular Engineering, University of Houston, Houston, Texas 77204, USA*
[2]*Department of Chemistry, University of Houston, Houston, Texas 77204, USA*
(Received 29 June 2017; published 23 August 2017)

We investigate the effects of geometric order and fluid rheology on the dispersion of micron-sized particles in two-dimensional microfluidic porous media. Particles suspended in a mixture of glycerol and water or in solutions of partially hydrolyzed polyacrylamide (HPAM) polymers were imaged as they flowed through arrays of microscale posts. From the trajectories of the particles, we calculated the velocity distributions and thereafter obtained the longitudinal and transverse dispersion coefficients. Particles flowed in the shear-thinning HPAM solution through periodic arrays of microposts were more likely to switch between streamlines, due to elastic instabilities. As a result, the distributions of particle velocity were broader in HPAM solutions than in glycerol-water mixtures for ordered geometries. In a disordered array of microposts, however, there was little difference between the velocity distributions obtained in glycerol-water and in HPAM solutions. Correspondingly, particles flowed through ordered post arrays in HPAM solutions exhibited enhanced transverse dispersion. This result suggests that periodic geometric order amplifies the effects of the elasticity-induced velocity fluctuations, whereas geometric disorder of barriers effectively averages out the fluctuations.

DOI: 10.1103/PhysRevE.96.022610

I. INTRODUCTION

Both fluid crowding and geometric confinement alter the transport of submicron particles through complex media [1–5]. This scenario appears across a broad range of technological and environmental settings: for example, when nanoparticles are used in enhanced oil recovery [6–9] to control the viscosity of aqueous solutions containing surfactants, salts, and polymers flowed into tight porous media; in bioremediation [10,11], to remove toxic organic compounds from water and wastewater; and in drug delivery [12–15], to convey therapeutic compounds through macromolecular fluids and the extracellular matrix to tissues within the human body. Because the efficacy of particles employed in these settings depends in part on their targeted transport, it is essential to understand how fluid properties and geometry affect the dispersion of submicron or nanosized particles.

In Newtonian fluids, particle dispersion is controlled by distinct mechanisms, depending on the relative rates of diffusion and convection as parameterized by the Péclet number (Pe), the ratio of the rate of diffusion to the rate of convection. When Pe is low (typically, for $\mathrm{Pe} < 6$), molecular diffusion controls the long-time dispersion of molecular tracers; conversely, when Pe is high (typically, for $\mathrm{Pe} > 72$), convective processes coupled weakly to diffusion control the long-time tracer dispersion [16,17]. The disordered structure [18] of the medium uniformly mixes the fluid, enabling the tracers to sample all positions within the bed [16]. Hence, dispersion at the macroscale has been traditionally defined in terms of macroscopic average parameters that describe the geometry of the porous medium, including tortuosity, porosity, and pore connectivity.

Deviations from this simple picture arise when the assumption that the particles can fully sample the pore space is violated. As one example, the periodicity in a geometrically ordered medium [19,20] can alter dispersion by generating deterministic [21,22] or time-periodic [23] particle trajectories or by coupling diffusive and advective transport on short-time and short-length scales [24]. As a second example, finite-size particles may be excluded from accessing the slow streamlines near the bounding surface [25], leading to early breakthrough in macroscopic measurements [26]. Finally, reducing the size of characteristic matrix length scales (e.g., a pore or throat size) brings particles, on average, closer to the bounding surface and hence may exacerbate the effects of particle-matrix interactions (including hydrodynamic [27–30] and/or physicochemical [29,31–33]) on particle transport. These examples suggest that processes at the pore scale ultimately control the ability of particles to spread throughout the porous medium. Thus, determining how specific features of pore-scale particle trajectories affect the macroscopic dispersion [34] is expected to improve understanding of the controlling physics.

The presence of dissolved fluid modifiers—such as the polymers used in oil production, the natural organic matter present in wastewater, or the macromolecules present in the extracellular fluid—further complicates understanding of particle dispersion in porous media. The dynamics of particles may directly couple to those of the crowders, especially when of similar size [35–37]. Moreover, in bulk flows such complex fluids often exhibit non-Newtonian rheology; confinement within a porous medium may alter fluid transport properties [38–40] and hence may also modify those of the particles. As one example, Darcy's law for flow in a porous medium posits that the flow rate increases linearly with the pressure gradient. Complex fluids flowed through a porous medium at a shear rate $\dot{\gamma}$ exceeding the characteristic relaxation rate of the fluid λ^{-1}, however, may experience pressure gradients that do not change linearly with the flow velocity [41], at variance with Darcy's law. This nonlinear response can lead to deviations from the flow profile of a Newtonian fluid even in a simple linear microchannel [42]. In more complex geometries, interactions between time- or

*ramanan@uh.edu
†jcconrad@uh.edu

rate-dependent flow properties of a complex fluid and the varying deformation imposed by a tortuous porous medium may lead to striking spatiotemporal variation in the local flow. This variation can manifest as flow instabilities, such as the elastic instabilities observed near cylinders confined within a microchannel [43,44]. These and other instabilities driven by non-Newtonian fluid rheology have been attributed to curved streamlines [2,45–47], interfacial instabilities [48], and/or shear banding [49]. In polymer solutions, these instabilities occur when the polymers are deformed faster than they can relax, i.e., at Weissenberg numbers $\mathrm{Wi} = \lambda\dot{\gamma} > 1$. Because elastic instabilities can drive exchange of fluid between areas of high viscosity (typically, near the centerline) and low viscosity (typically, near walls) [50], they may promote the switching of particles from one streamline to another and hence increase particle dispersion in porous media. It is not obvious, however, that instabilities will enhance dispersion—alternatively, the non-Newtonian fluid characteristics may be effectively averaged out by flow through a disordered medium [40]. Indeed, contrasting effects on particle dispersion are reported in geometrically ordered two-dimensional (2D) porous media (in which polymer additives enhance transverse dispersion) [3] and in geometrically disordered 3D porous media (in which polymer additives do not alter transverse dispersion) [4]. This comparison suggests that how the coupling between fluid rheology and local geometry affects particle dispersion remains incompletely understood.

Here, we show using pore-scale experiments that geometry and fluid viscoelasticity impart distinct features to the dispersion of microscale particles in 2D microfluidic porous media. Particles suspended in Newtonian mixtures of glycerol and water and in shear-thinning polymeric solutions of partially hydrolyzed polyacrylamide (HPAM) were flowed through micropost arrays of varying geometries, and their trajectories were obtained using imaging processing methods. Longitudinal dispersion was not affected by either post geometry or fluid nature. By contrast, the transverse dispersion of particles flowed in the HPAM solution was increased in ordered post arrays but not in randomly distributed post arrays. At the pore scale, the enhanced transverse dispersion likely originated from the increased probability that particles switched between streamlines when flowed in the polymer solution, leading to a broadening of the velocity distributions and an increase in the velocity fluctuations.

II. MATERIALS AND METHODS

A. Particle suspensions

An aqueous solution containing 0.1% (w/w) hydrolyzed polyacrylamide (HPAM) was prepared by dissolving as-received FLOPAAM 3330 (M_w = 8 MDa, purchased from SNF) in deionized water. Fluoro-Max red fluorescent polystyrene nanoparticles of diameter $d_p = 2$ μm (1% w/w, Thermo Fisher Scientific) were suspended in the HPAM solution and in a 90% glycerol-water (w/w) mixture, and the suspensions were tumble-rolled for 24 h to ensure thorough homogenization. The rheology of these solutions was characterized using a Discovery Hybrid Rheometer (DHR-2, TA Instruments) equipped with a single Couette cell of

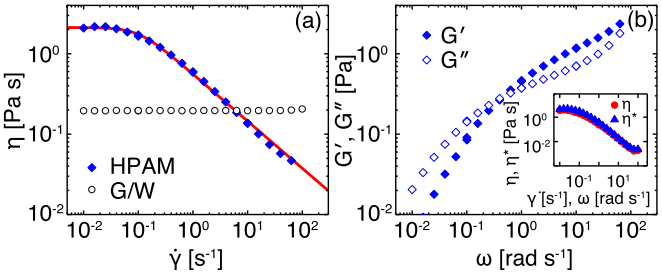

FIG. 1. (a) Steady-shear viscosity as a function of shear rate for the 0.1% HPAM (closed diamonds) and 90% glycerol (open circles) solutions. The red line represents a fit to the Carreau model, Eq. (1). (b) Linear dynamic oscillatory shear-based elastic (G', closed) and viscous (G'', open) moduli of the 0.1% HPAM solution as a function of angular frequency ω. Inset: the complex viscosity η^* and the viscosity η obey an empirical Cox-Merz rule [51].

cup diameter 30.36 mm, bob diameter 27.97 mm, and bob length 41.89 mm; the gap size was 4 mm. Rheological characterizations of both solutions are shown in Fig. 1. The viscosity of the glycerol-water solution, 0.2 Pa s, was independent of shear rate. For the HPAM solution, a plateau in the viscosity was observed at low shear rates. Rheological data were fit to the Carreau model,

$$\mu = \mu_\infty + (\mu_0 - \mu_\infty)[1 + (\lambda\dot{\gamma})^2]^{(n-1)/2}, \qquad (1)$$

from which we obtained a high-shear viscosity $\mu_\infty = 0.001$ Pa s, a zero-shear viscosity $\mu_0 = 2.1$ Pa s, a power index $n = 0.42$, and a longest relaxation time $\lambda = 15$ s. The complex viscosity η^* (as a function of angular frequency ω) and the steady-shear viscosity η (as a function of shear rate $\dot{\gamma}$) of the HPAM solution obeyed an empirical Cox-Merz rule [51].

B. Microfluidic channels

Polydimethylsiloxane (PDMS, Sylgard 184, Dow Corning) microfluidic channels of width 1000 μm, length 30 mm, and height 8 μm were fabricated using soft lithography. Posts of diameter 15 μm were arranged over a 2000 × 1000 μm area in: (i) regular (periodic) square arrays, oriented at an angle of 0° or 45° with respect to the incident flow (velocity) direction; (ii) a regular (periodic) hexagonal array; and (iii) a randomly distributed (aperiodic) array [Figs. 2(a)–2(d)]. In the periodic arrays, the edge-to-edge spacing between the posts with ordered arrays was fixed at 15 μm (giving porosities of 0.80 and 0.77 for the square and hexagonal lattices, respectively); in the random array, the average edge-to-edge spacing between posts was 39 μm (giving porosity of 0.95) [Table I in Appendix A].

The inlet and outlet ports on the PDMS microchannel were made using a biopsy punch (Miltex I.D., 1.0 mm). To seal the microfluidic device, the PDMS was exposed to oxygen plasma and subsequently bonded to a 48 × 65 mm cover glass (Gold Seal). The device was then connected to a mechanical (constant-displacement) syringe pump using Microbore PTFE tubing (0.022-in ID and 0.042-in OD, Cole-Palmer). In our experiments, the flow rate was varied from 0.1–0.6 μl min^{-1}. In the different geometries, we accessed Péclet numbers in the range $3 \times 10^3 < \mathrm{Pe} < 2 \times 10^6$ for the 90% glycerol-water

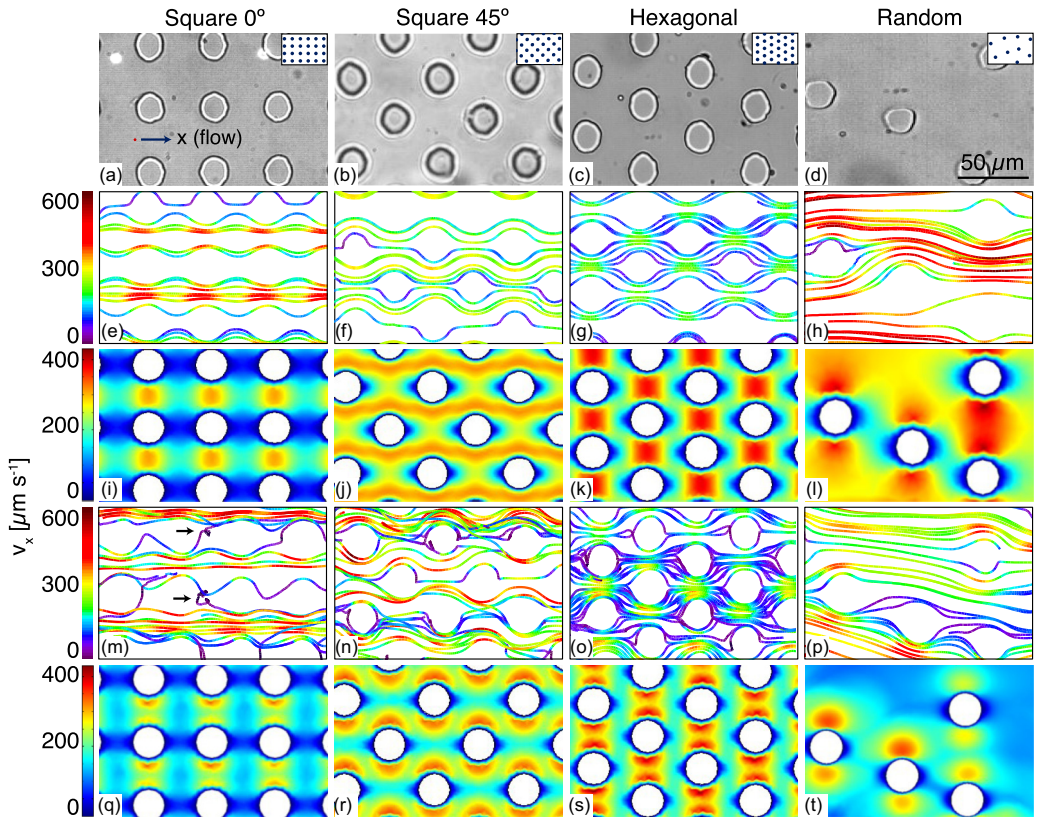

FIG. 2. (a–d) Brightfield micrographs of the post arrays used in the experiments. Angles indicate the orientation of the director relative to the incident flow (along x). The red dot in (a) indicates the size of the particles relative to the post array. (a) Square 0° post array. (b) Square 45° post array. (c) Hexagonal post array. (d) Randomly distributed post array. (e–h, m–p) Representative trajectories of 2 μm PS particles and (i–l, q–t) COMSOL finite-element simulations of flow in the post arrays. The average velocity ~250 μm s^{-1} is constant in all images. In (e–l), the fluid was 90% glycerol-water: (e, i) square 0° array (experimental flow rate: 0.4 μl min^{-1}); (f, j) square 45° array (0.6 μl min^{-1}); (g, k) hexagonal array (0.6 μl min^{-1}); (h, l) randomly distributed array (0.3 μl min^{-1}). In (m–t), the fluid was 0.1% HPAM: (m, q) square 0° array (0.3 μl min^{-1}); (n, r) square 45° array (0.3 μl min^{-1}); (o, s) hexagonal array (0.2 μl min^{-1}); (p, t) randomly distributed array (0.1 μl min^{-1}). The colorbars in (e–t) indicate the magnitude of the longitudinal velocity v_x. The scale bar for all images [shown in (d)] is 50 μm. The black arrows in (m) indicate recirculating trajectories.

solution [Table II in Appendix A]; in the HPAM solution, we accessed Péclet numbers (based on the zero-shear viscosity of the solution) in the range $5 \times 10^4 < \mathrm{Pe} < 5 \times 10^6$ [Table III in Appendix A] and Weissenberg numbers in the range $18 < \mathrm{Wi} < 2000$ [Table IV in Appendix A]. Here $\mathrm{Pe} = \langle v_x \rangle d_p / D_0$, where $\langle v_x \rangle$ was the average velocity in the flow (x) direction, d_p was the particle diameter, and D_0 was the particle diffusivity measured in quiescent conditions.

C. Imaging and particle tracking

Particle motion during flow was imaged using a Leica SP8 inverted microscope and a high-speed camera (AOS Technologies). All movies were acquired in the center of the post array, to avoid entrance or exit effects, and at a fixed height of 4 μm above the coverslip (i.e., at the vertical midplane of the channel). Videos were recorded at frames rates of 32–500 frames s^{-1} (fps) at a resolution of 640 × 480 pixels, which covered an area of 307.2 × 230.4 μm^2. The centroids of the particles were located in each image with a resolution of $\varepsilon = 100$ nm [52] and linked into trajectories using a single-particle tracking algorithm. Any particles that irreversibly adhered to the posts were excluded from further analysis.

TABLE I. Areal density and porosity of the post arrays.

Geometry	Areal density [posts μm^{-2}]	Porosity
Square	0.0019	80
Hexagonal	0.0016	77
Random	0.003	95

TABLE II. Péclet number $\times 10^4$ of nanoparticles in glycerol-water flowed through post arrays as a function of the imposed flow rate.

Flow rate [μl min^{-1}]	0.1	0.2	0.3	0.4	0.5	0.6
Square 0°	0.37	0.85	3.3	39	79	133
Square 45°	3.9	5.4	9.8	19	38	56
Hexagonal	9.4	14	18	19	20	21
Random	43	59	82	110	130	140

TABLE III. Péclet number $\times 10^4$ of nanoparticles in HPAM solution flowed through post arrays as a function of the imposed flow rate.

Flow rate [μl min^{-1}]	0.1	0.2	0.3	0.4	0.5	0.6
Square 0°	5.0	76	120	200	230	
Square 45°	28	75	92	110	220	260
Hexagonal	51	110	180	210	211	230
Random	130	280	340	480	530	

D. Metrics

The distributions of the velocities of the particles flowing through the post arrays were calculated from the measured particle trajectories. At least 50 (square 0° array) or 100 (all other arrays) distinct trajectories, containing 20 000–30 000 points, were analyzed for each combination of post arrangement and solution type. To quantitatively assess the extent of particle dispersion, time-dependent longitudinal ($D_L(t)$, along the direction of flow, x) and transverse ($D_T(t)$, normal to the direction of flow, y) dispersion coefficients were calculated as

$$D_{L,T}(t) \equiv \frac{1}{2}\frac{d\sigma^2_{L,T}}{dt} = \int_0^t C_{L,T}(t')dt', \qquad (2)$$

where $\sigma^2_{L,T}(t)$ is the second moment of particle displacements in the longitudinal or transverse direction, respectively. $C_{L,T}(t)$ is the time-dependent velocity autocovariance, approximated as

$$C_{L,T}(t) = \sum_{i=1}^{N}(v_{xi,yi}(t) - \langle v_{x,y}\rangle)(v_{xi,yi}(0) - \langle v_{x,y}\rangle). \qquad (3)$$

In Eq. (3), $v_{xi,yi}(t)$ is the longitudinal or transverse velocity of particle i, respectively, at a time t, $v_{xi,yi}(0)$ is the longitudinal or transverse velocity of particle i, respectively, at the start of its trajectory, and $\langle v_{x,y}\rangle$ is the average longitudinal or transverse velocity, calculated over all N particles and all times [53]. If $d\sigma^2_{L,T}/dt$ is a constant, then the dispersion coefficients obtained from the classical advection-dispersion equation are recovered [53]. In this manuscript, we applied the second equality and calculated the dispersion coefficient through the approximate velocity autocovariance. We confirmed that the value of the dispersion coefficient obtained this route [i.e., through the second equality in Eq. (2)] equalled that obtained by numerically differentiating the second moment of particle displacements (i.e., through the first equality in Eq. (2), shown for a representative example in Fig. 9 in Appendix B).

TABLE IV. Weissenberg number of nanoparticles in HPAM solution flowed through post arrays as a function of the imposed flow rate.

Flow rate [μl min^{-1}]	0.1	0.2	0.3	0.4	0.5	0.6
Square 0°	19	280	450	730	880	
Square 45°	110	280	340	410	830	970
Hexagonal	190	420	680	780	790	860
Random	470	1100	1300	1800	2000	

Dispersion coefficients were normalized by the diffusivity of the particles, D_0, measured in quiescent conditions. The lag time t was normalized by the characteristic advective time scale $d_c/\langle v_x\rangle$, where d_c is the post diameter.

E. Numerical simulations

Fluid flow was simulated using a 2D laminar flow model in COMSOL Multiphysics 4.1. The computational model consists of a 200 × 200 μm box that contains circles of diameter 15 μm that were spaced by 15 μm in various periodic arrangements or on average by 39 μm in a random medium, to match the experiments. Using the shallow channel approximation, the height of the system was set to 8 μm. The 90% glycerol-water solution was modeled as a Newtonian fluid with a constant viscosity of 0.2 Pa s. The non-Newtonian HPAM solution was modeled as a Carreau fluid [cf. Eq. (1)], using as parameters the experimentally measured high-shear viscosity $\mu_\infty = 0.001$ Pa s, zero-shear viscosity $\mu_0 = 2.1$ Pa s, power index $n = 0.42$, and longest relaxation time $\lambda = 15$ s.

III. RESULTS AND DISCUSSION

A. Flow profiles within model porous media

Using imaging and single-particle tracking, we obtained the trajectories of particles suspended in a Newtonian glycerol-water solution and in a shear-thinning polymer HPAM solution as they flowed through random (aperiodic) or ordered (periodic) post arrays [Figs. 2(a)–2(d)]. Both the arrangement of the posts and the presence of the polymers in solution qualitatively affected the flow profiles of the particles. In the glycerol-water mixtures, particles flowed through ordered arrays of posts following laminar streamlines that symmetrically diverged around the posts [Figs. 2(e)–2(g)]. Notable differences in the local velocity were observed as a function of post arrangement. In the 0° square array, for example, stagnation zones appeared in the regions behind the posts along the direction of flow [Fig. 2(e)], consistent with earlier studies [54]. These regions were largely inaccessible to the particles, which tended to follow linear or gently curved streamlines through the broad open channels running through the post array. Stagnation zones did not appear in the other ordered arrays [e.g., the 45° square array, Fig. 2(f), or the hexagonal array, Fig. 2(g)], which lacked the open channels that allowed particles to follow nearly straight and unimpeded streamlines. In the disordered array [Fig. 2(h)], particles exhibited high velocities near the posts and in open regions within the array. In all arrays, the velocity profiles of the particles measured in experiments were in qualitative agreement with velocity profiles of the fluid that were calculated using the finite-element simulation package COMSOL [Figs. 2(i)–2(l)].

Similarly, modifying the rheology of the fluid from Newtonian to viscoelastic led to qualitative changes in the fluid flow and in particle trajectories. Particles suspended in the shear-thinning HPAM solution exhibited locally higher velocities nearer the posts than in the pore center [Figs. 2(m)–2(p)], consistent with the locally higher fluid velocities observed there in the COMSOL simulations [Figs. 2(q)–2(t)]. This finding is consistent with earlier studies showing that polymer solutions experience shear flow (and thus, for shear-thinning solutions,

a lower viscosity) near the walls in a converging-diverging flow field [55–58], such as that found in a porous medium. Further, the trajectories of particles in HPAM solutions were noticeably less smooth and more asymmetric. This asymmetry suggested that particles flowed in the viscoelastic and shear-thinning polymer solution could switch from one streamline to another. As one consequence, the stagnation zones that were rarely populated by particles in the glycerol-water solution became accessible to particles in the HPAM solution. Particle trajectories in these regions, indicated by arrows in Fig. 2(m), revealed an unstable and recirculating flow.

These changes in the particle trajectories are consistent with earlier observations of flow features arising from the viscoelasticity of the polymer solution. Elastic instabilities that occur when polymer solutions flow through confined geometries are known to generate fluctuations in streamlines [54], and additionally cause local pressure variations that lead to temporary pressure gradients in otherwise stagnant areas [43,59] and enhance mixing [60]. These instabilities typically appear at Weissenberg numbers greater than 1, with the value of the onset depending on geometry. In our experiments, $\mathrm{Wi} > 10^2$ [Table IV in Appendix A]; hence, it is likely that nonlinearities in flow arising from the deformation of the polymer fluid were sufficient to alter the particle trajectories. Similarly, unstable recirculation regions in the stagnation zones were observed in the spaces between posts in earlier studies of Boger [59,61–63] and shear-thinning [54] fluids flowed through post arrays.

B. Streamline switching in particle trajectories

The trajectories displayed in Fig. 2 suggest that fluid elasticity may enable particles to reach previously inaccessible regions within the porous medium. To separate the effects of fluid elasticity and geometry on the mechanisms underlying this increase in void accessibility, we contrasted representative individual trajectories of particles suspended in the Newtonian glycerol-water mixture or in the viscoelastic HPAM solutions and flowed through the square arrays. In a square array oriented 0° with respect to the flow direction, particles in glycerol-water nearly always followed a single streamline as they traversed the microscopic field of view (of length 307.2 μm) and exhibited periodic trajectories [Fig. 3(a)]. Both the velocities in the x and y directions, v_x and v_y, and the associated velocity fluctuations, $v_x^2/\langle v_x^2\rangle$ and $v_y^2/\langle v_y^2\rangle$, featured regular oscillations as particles traversed the ordered post arrays. Particles could switch from one streamline to another only when following a streamline that closely approached a post [Fig. 3(b)]. Similar trajectories were observed for particles flowing through a square array that was tilted 45° with respect to the incident flow. Again, most particles followed a single streamline through the field of view [Fig. 3(c)] and could switch streamlines only upon directly encountering a post [Fig. 3(d)]. As the direct encounter rate was relatively rare, only 1% of particles in the 0° array and 5% of particles in the 45° array exhibited at least one switch in the field of view.

By contrast, particles flowed in the shear-thinning HPAM solution were significantly more likely to jump from one streamline to another within a microscopic field of view. Although some particles indeed followed a single streamline

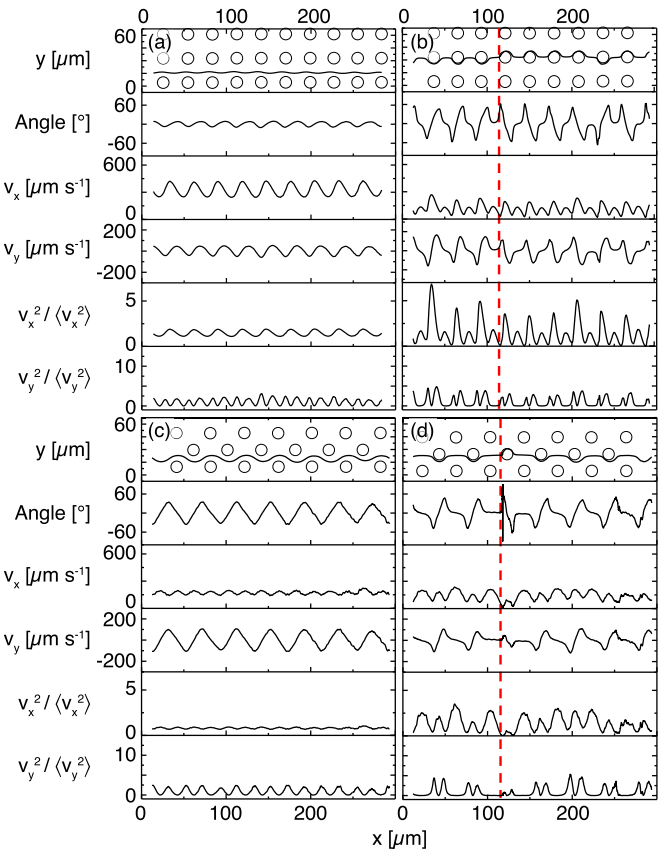

FIG. 3. Example trajectories of 2-μm particles in 90% glycerol-water solution that were flowed through square arrays oriented 0° [(a) and (b), 0.4 μl min^{-1}] or 45° [(c) and (d), 0.6 μl min^{-1}] with respect to the flow. From top to bottom in each panel: position, velocity angle, longitudinal velocity v_x, transverse velocity v_y, longitudinal velocity fluctuations $v_x^2/\langle v_x^2\rangle$, and transverse velocity fluctuations $v_y^2/\langle v_y^2\rangle$. The selected particles had similar average velocities ($\sim$250 μm s^{-1}). The vertical dashed lines in (b) and (d) indicate the horizontal position at which the particle switched from one streamline to another. The value $x = 0$ is not physically meaningful.

down a relatively open channel [Figs. 4(a) and 4(d)], some particles migrated from the centerline to areas near the post walls [Figs. 4(b) and 4(e)] in both the square 0° and 45° arrays. This migration required the particles to switch streamlines. As a result, 31% of particles in the square 0° array and 36% of the particles flowed through the square 45° array switched streamlines at least once while in the field of view. The change from one streamline to another was signaled by an abrupt change in the periodicity of the particle's direction of motion (velocity angle) and coincided with enhanced velocity fluctuations, especially in the y direction. Moreover, many of these abrupt changes occurred when particles were close to the region of high velocity (and hence high shear rate) near the particle posts. Particles that spent significant time in the regions behind from the posts, which featured unstable and/or recirculating flows, exhibited high velocity fluctuations [Figs. 4(c) and 4(f)]; upon leaving these regions, the trajectories became more regular. Increases in the fluctuations of particle velocities with shear rate were observed in similar microfluidic experiments [3].

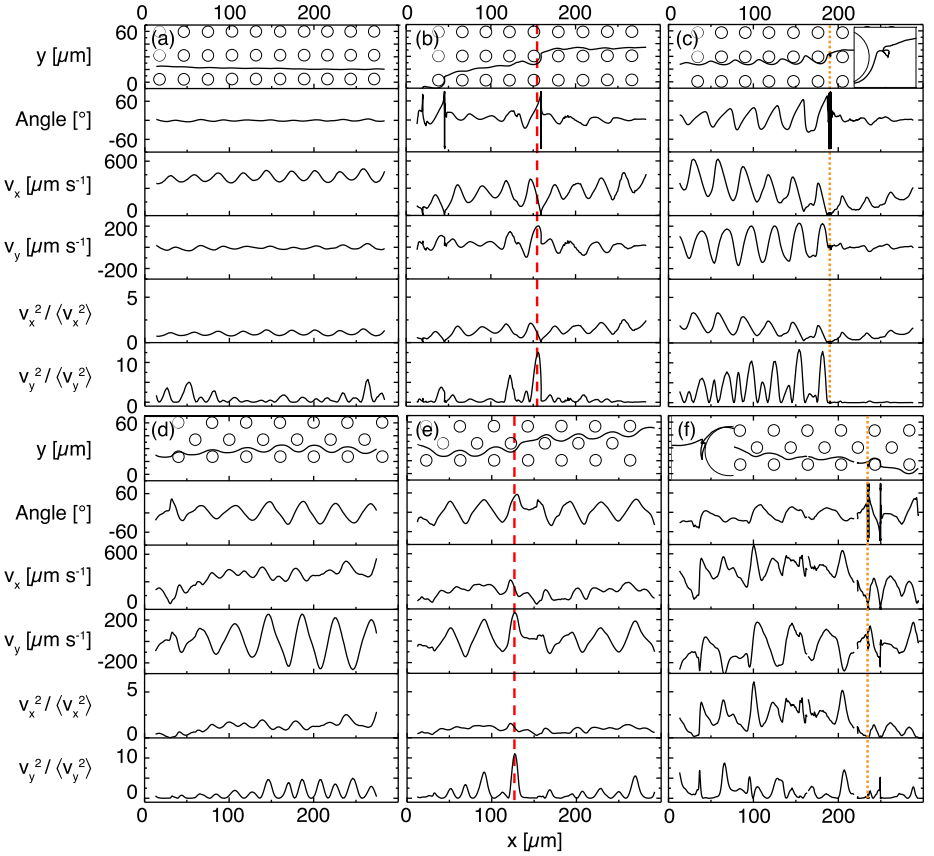

FIG. 4. Example trajectories of 2-μm particles in 0.1% HPAM solution that were flowed through square arrays oriented 0° [(a)–(c), 0.6 μl min^{-1}] or 45° [(d)–(f), 0.6 μl min^{-1}] with respect to the flow. From top to bottom in each panel: position, velocity angle, longitudinal velocity v_x, transverse velocity v_y, longitudinal velocity fluctuations $v_x^2/\langle v_x^2\rangle$, and transverse velocity fluctuations $v_y^2/\langle v_y^2\rangle$. The selected particles had similar average velocities ($\sim$250 μm s^{-1}). The vertical dashed lines in (b) and (e) indicate the horizontal position at which the particle switched from one streamline to another; the vertical dotted lines in (c) and (f) indicate the horizontal position at which the particle interacted with the stagnant recirculating regions downstream of the posts. The insets in (c) and (f) highlight segments of each particle trajectory that exhibit recirculation. The value $x = 0$ is not physically meaningful.

C. Velocity profiles

Inspection of the trajectories of particles that switch streamlines suggested that velocity fluctuations promote lateral particle migration, in accordance with earlier studies [3]. Because spatial [64] and temporal [65] velocity fluctuations are increased in shear-thinning fluids, we therefore compared the distributions of normalized longitudinal ($v_x/\langle v\rangle$) and transverse ($v_y/\langle v\rangle$) velocities for the glycerol-water and polymer solutions in random and in square arrays; here $\langle v\rangle$ represents the average velocity calculated across all trajectories for a given flow rate and post configuration. First, we examined the distributions of velocities at the lowest bulk flow rate, 0.1 μl min^{-1}. In the longitudinal (x) direction, the normalized velocity distribution for all post configurations was centered at $v_x/\langle v\rangle > 0$, indicating net convective motion in the direction of flow [Figs. 5(a)–5(f)]. All distributions were non-Gaussian [66], suggesting that both convective and diffusive processes contributed to the distributions of particle velocity [24]. The transverse (y) velocity distributions at this flow rate were symmetric, indicating that the particles did not have a preferred direction normal to the flow [Figs. 5(g)–5(l)]. The shapes of the longitudinal distributions for particles in glycerol-water were similar for the random and square 0° arrays [Figs. 5(a), 5(c) and 5(e)], with a small fraction of particles exhibiting negative velocities; the distribution for the square 45° array was shifted to slightly higher velocities. In all distributions, the sharp local maximum near zero velocity reflected the contributions from two processes: (i) particles that closely approached the surface of a post, or (ii) particles that were trapped inside recirculation zones. The shape of the transverse velocity distribution was clearly distinct for all three arrays [Figs. 5(g), 5(i) and 5(k)], with the distributions in the square arrays exhibiting sharp maxima centered at zero. This result indicated that the post arrangement was sufficient to alter the velocity distributions of the particles. Even more pronounced differences were observed between the longitudinal [Figs. 5(b), 5(d) and 5(f)] and transverse [Figs. 5(h), 5(j) and 5(l)] velocity distributions of particles in HPAM solutions in the three different geometries. Even at the lowest flow rate (0.1 μl min^{-1}), the Weissenberg number of the HPAM solution exceeded 20 [Table IV in Appendix A], so that the polymer chains were at least slightly deformed at all flow rates and suggesting that stresses generated [67] may affect the particle motions. Indeed, for a given geometry the

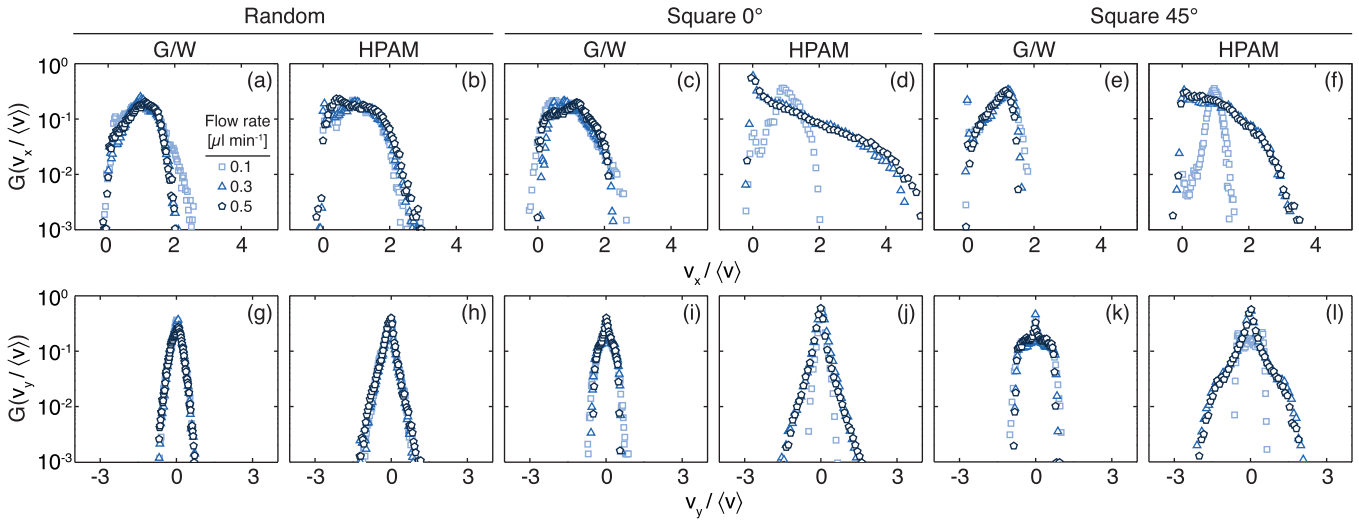

FIG. 5. Distributions of normalized longitudinal (x, top row) and transverse (y, bottom row) velocities of 2 μm particles in (a, c, e, g, i, k) 90% glycerol-water or (b, d, f, h, j, l) 0.1% HPAM solutions in post arrays of various configurations. Post configuration: (a, b, g, h) random array; (c, d, i, j) square 0° array; (e, f, k, l) square 45° array. Symbols indicate flow rates: 0.1 μl min^{-1} (squares), 0.3 μl min^{-1} (triangles), 0.5 μl min^{-1} (pentagons).

distributions in glycerol-water and HPAM were dissimilar and could not be scaled onto one another, indicating that the fluid rheology also altered the velocity distributions.

To test the idea that increasing the shear rate enhances the velocity fluctuations of particles in the shear-thinning polymer solution, we examined the normalized velocity distributions at higher flow rates. In the random array, for a given fluid rheology the longitudinal and transverse distributions for different flow rates collapsed onto a master curve as a function of the normalized velocities $v_x/\langle v\rangle$ or $v_y/\langle v\rangle$ [Figs. 5(a), 5(b) 5(g), and 5(h)]. The scaling curves differed slightly for the Newtonian glycerol-water and for the shear-thinning HPAM solution; the modest broadening of the HPAM curve relative to that for glycerol-water was consistent with larger velocity fluctuations in the polymer solution, likely due to stresses arising as the polymers' conformations are deformed by the flow [67]. These results, obtained in a random 2D array, are similar to those obtained earlier by us in 3D random porous media [4]. In that study, we suggested that the disordered structure of the 3D packed bed effectively averaged out any fluctuations arising from the polymer fluid viscoelasticity. Here, we similarly conclude that the presence of polymer additives does not significantly modify the velocity distributions in open disordered 2D media.

In the square arrays, the velocity distributions for particles in glycerol-water solutions also collapsed onto a master

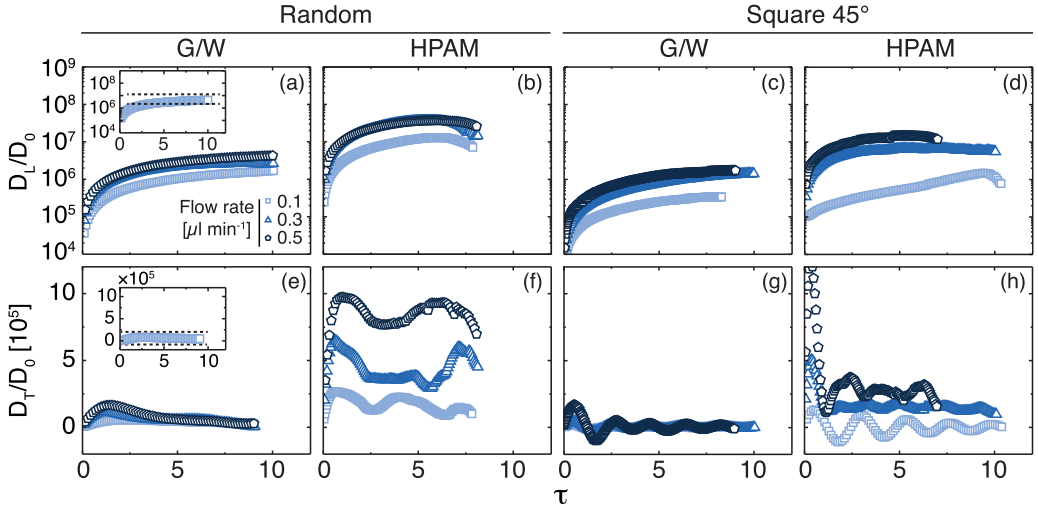

FIG. 6. Normalized longitudinal [$D_L(\tau)/D_0$ (a–d)] and transverse [$D_T(\tau)/D_0$ (e–h)] dispersion coefficients as a function of the normalized lag time $\tau = t\langle v_x\rangle/d_c$ for 2 μm particles in 90% glycerol-water (a, c, e, g) or 0.1% HPAM (b, d, f, h) solutions. The posts were randomly oriented (a, b, e, f) or arranged in a square lattice oriented 45° with respect to the incident flow (c, d, g, h). The insets in (a) and (e) illustrate how error bounds on the asymptotic dispersion value were obtained for one set of data (particles in glycerol-water flowed at 0.5 μl min^{-1} through a random array). Symbols indicate flow rates: 0.1 μl min^{-1} (squares), 0.3 μl min^{-1} (triangles), 0.5 μl min^{-1} (pentagons).

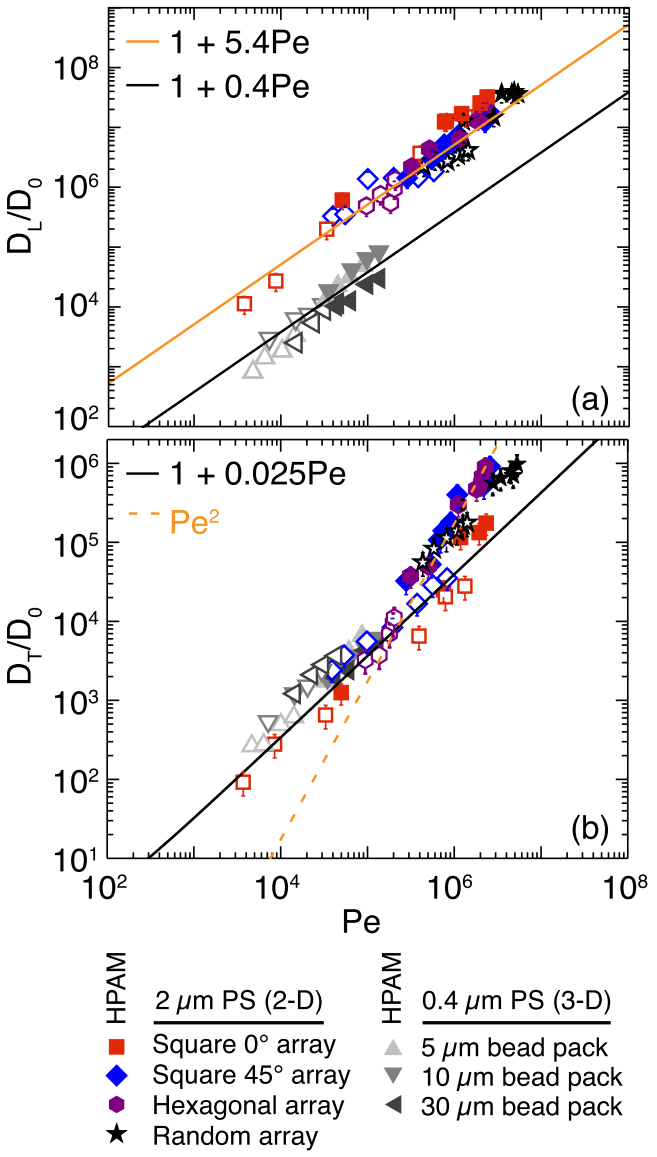

FIG. 7. Normalized asymptotic (a) longitudinal (D_L/D_0) and (b) transverse (D_T/D_0) dispersion coefficients as a function of Péclet number Pe. The data for the 0.4 μm PS particles in glass bead packed beds is taken from Ref. [4]. Error bars indicate the bounds on the asymptotic coefficients estimated from the time-dependent dispersion functions as illustrated in Fig. 6.

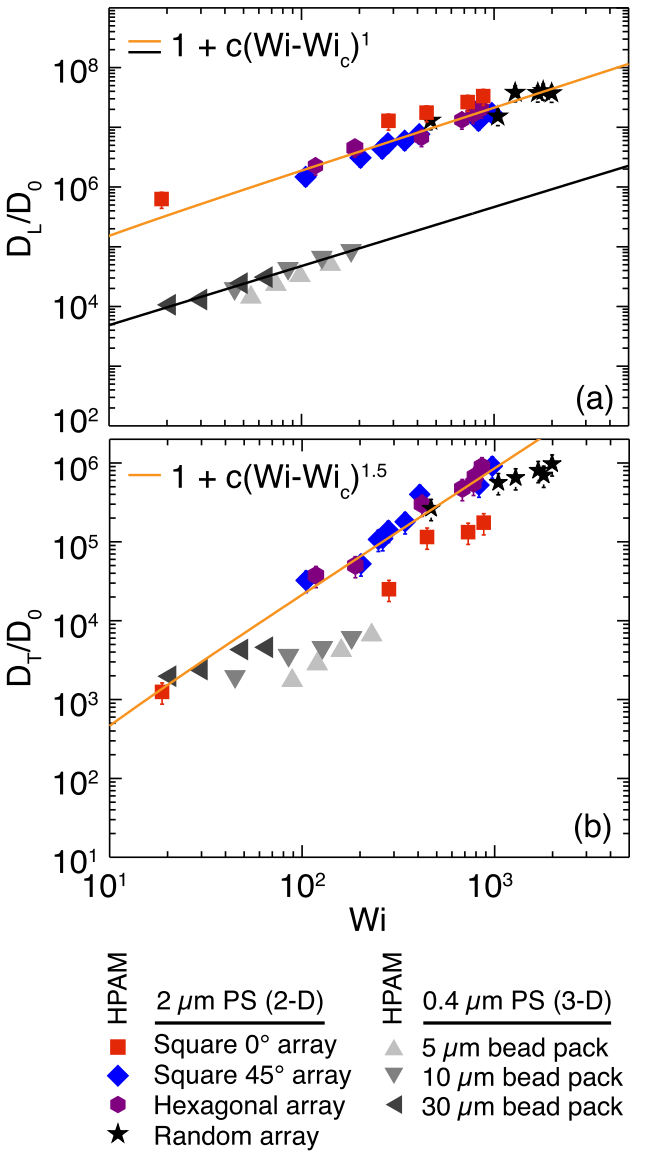

FIG. 8. Normalized asymptotic (a) longitudinal (D_L/D_0) and (b) transverse (D_T/D_0) dispersion coefficients as a function of Weissenberg number Wi. In both panels, Wi_c is set to 1. The data for the 0.4 μm PS particles in glass bead packed beds is taken from Ref. [4]. Error bars indicate the bounds on the asymptotic coefficients estimated from the time-dependent dispersion functions as illustrated in Fig. 6.

curve for a given post orientation. The scaling curves for the square 0° and 45° arrays were distinct, reflecting the preferential direction of transport imposed by the underlying geometric ordered structure [22]. In contrast to the clean scaling collapses observed for the glycerol-water experiments, pronounced deviations from universal scaling were observed for the velocity distributions of particles flowed in HPAM solutions. The normalized velocity distributions for the two highest flow rates were markedly broader for particles flowing through both the 0° and 45° arrays in both longitudinal and transverse flow directions [Figs. 5(d), 5(f) 5(j), and 5(l)]. This result suggests that the regular periodic order in these post arrays amplified the velocity fluctuations as the polymer solution was increasingly deformed, consistent with earlier measurements for HPAM solutions in 2D ordered arrays [3] but in contrast to our result for the random 2D post array (current study) and that obtained in our earlier study of disordered (3D) packed beds [4].

D. Dispersion coefficients

Together, Figs. 4 and 5 suggest that fluid viscoelasticity coupled to periodic geometric structure lead to enhanced velocity fluctuations that, in turn, are expected to increase dispersion, especially in the transverse direction. To test this idea, we calculated time-dependent longitudinal and transverse dispersion coefficients from the particle trajectories

using Eqs. (2) and (3). For both random and periodic arrangements of posts and for glycerol-water and HPAM solutions, the normalized longitudinal dispersion coefficients of the particles $D_L(\tau)/D_0$ increased with the normalized lag time $\tau = t\langle v_x\rangle/d_c$ on short time scales (where d_c is the post diameter) and approached an asymptotic value on long time scales ($4 \leqslant \tau \leqslant 10$) [Figs. 6(a)–6(d)]. The time scale required to reach the asymptote, on which the longitudinal autocorrelation function $C_L(\tau)$ approached zero [Fig. 10], was set by convection [53,68]. From the time-dependent dispersion curves, we extracted the long-time asymptotic value D_L/D_0 that described the longitudinal dispersion in each array and fluid and determined error bounds as shown in the inset to Fig. 6(a).

The normalized transverse dispersion coefficients $D_T(\tau)/D_0$ initially increased with τ on short time scales, attaining a local maximum, and then decreased on longer time scales [Figs. 6(e)–6(h)]; the decrease reflected contributions from particles that sampled regions of relatively slow flow within the porous medium [69]. The normalized time corresponding to the maximum was in approximate agreement with the theoretical prediction, $\tau = \sqrt{1-\phi} \approx$ 0.2–0.5, calculated from the porosity $\phi \approx 0.77$–0.95 of the post arrays [70]. In the random array, the transverse dispersion coefficients of particles flowing in glycerol-water decreased monotonically to an asymptote at long time scales [Fig. 6(e)]. In HPAM solutions, $D_T(\tau)/D_0$ in the random array fluctuated around an average value, as also observed in earlier studies [65]. The fluctuation in $D_T(\tau)/D_0$ reflected oscillations in the velocity autocorrelation function [Fig. 9 in Appendix B], which likely arose from the viscoelasticity of the polymer solution.

In the ordered square arrays, $D_T(\tau)/D_0$ oscillated in time for both glycerol-water and HPAM, reflecting the periodicity of the array [3]. Negative values of $D_T(\tau)/D_0$ result from negative values of the velocity autocorrelation function from which they are calculated [Fig. 10 in Appendix B], and likely reflect contributions from particles that follow streamlines around obstacles in the flow field to gradually reduce their transverse displacements on intermediate time scales [53]. Particles flowing in glycerol-water at all flow rates and in HPAM at the lowest flow rate exhibited smoothly-decaying oscillations with a similar period of oscillation, set by the post arrangement: the distance between the first maximum and minimum in this oscillation, $\langle v_x\rangle t \approx 15\,\mu$m, coincided with the edge-to-edge distance between posts [Fig. 11 in Appendix B]. The dispersion coefficient of particles flowed at higher rates through HPAM solutions, however, exhibited irregular oscillations on longer time scales, consistent with the idea that the velocity fluctuations were enhanced by the fluid viscoelasticity. Because the persistent oscillations in the transverse dispersion coefficients complicated the extraction of the long-time asymptotic value, we also calculated the transverse mean-square displacement ($\mathrm{MSD}_\perp$) as a function of lag time. The dispersion coefficients calculated from the long-time linear portion of $\mathrm{MSD}_\perp$ were in good agreement with those extracted from the long-time asymptotic value of D_T/D_0, validating our approach [Fig. 9 in Appendix B].

We first examined the dependence of the long-time asymptotic values D_L/D_0 and D_T/D_0 on the Péclet number $\mathrm{Pe} = \langle v_x\rangle d_p/D_0$, where d_p is the particle diameter. Our 2D experiments spanned Péclet numbers $3 \times 10^3 < \mathrm{Pe} < 5 \times 10^6$ and thus accessed the pure mechanical dispersion regime ($300 < \mathrm{Pe} < 10^7$), in which molecular diffusion negligibly affects the spreading of particles [71,72]. In this regime, both D_L/D_0 and D_T/D_0 are expected to increase linearly with Pe. Indeed, we found that D_L/D_0 increased approximately linearly with Pe for all fluids and all post configurations, in agreement with this expectation [Fig. 7(a)]. Dispersion coefficients obtained in 3D random media from Ref. [4] are also shown for comparison; the prefactor was lower but the scaling exponent was similar, likely reflecting differences in the dimensionality (3D) and porosity ($\phi \approx 0.35$) of the medium. (Scaling collapses of dispersion coefficients as a function of Pe [72] show a similar spread across different experimental configurations.) Likewise, in glycerol-water solutions the transverse dispersion coefficient D_T/D_0 increased linearly with Pe [Fig. 7(b)] for all post configurations.

The dispersion coefficients of particles in the non-Newtonian fluid, however, appeared to depend on the arrangement of the posts. In all post arrays, D_T/D_0 scaled linearly at low Pe. For the random posts (closed stars) this linear scaling persisted at higher Pe, although the values of D_T/D_0 were somewhat higher than those measured for other configurations. In geometrically ordered 2D arrays, however, D_T/D_0 scaled nonlinearly with Pe at high Péclet numbers, implying that other processes contributed to transverse dispersion in this limit (when the molecular diffusion time scale is very long due to addition of polymers to solution). For all ordered arrays except the 0° square array, D_T/D_0 scaled as Pe^2 in the high Péclet number limit. In the 0° array, D_T/D_0 scaled as Pe^α, with $1 < \alpha < 2$; given the limited range of Pe accessed, we were unable to determine the scaling exponent more precisely for these experiments. We note, however, that a key difference between flow in the square 0° array and that in the other ordered arrays was the extent of the streamline curvature imposed by the post arrangement—the square 0° array featured large open channels through which the polymer solution could flow without distortion. Large streamline curvatures or other extensional forces that stretch the polymer molecules can generate elastic instabilities in flow [44]. Because relatively few streamlines interact with the posts in the square 0° array (relative to the staggered ordered arrays), it is likely that the elastic instabilities that promote streamline crossing and transverse particle migration are reduced in this geometry.

Next, we examined the scaling behavior of the dispersion coefficients in HPAM solutions with the Weissenberg number $\mathrm{Wi} = \lambda\dot{\gamma} = \lambda\langle v_x\rangle/h$, where $\dot{\gamma} = \langle v_x\rangle/h$ is the average (2D) shear rate in the fluid and h is the height of the channel. The Weissenberg number describes the onset of stress anisotropy [73]; in sheared polymer solutions, Wi characterizes the anisotropy in the alignment of the polymers [3]. Both D_L/D_0 and D_T/D_0 increased with Wi [Fig. 8]. The longitudinal coefficients D_L/D_0 scaled linearly with Wi. In the 2D microfluidic experiments described here, all data collapsed onto a master scaling curve; the dispersion coefficients obtained for flow through a 3D packed bed in Ref. [4] scaled onto a different master curve, with a similar slope but shifted to lower values of Wi. This result suggests that the arrangement

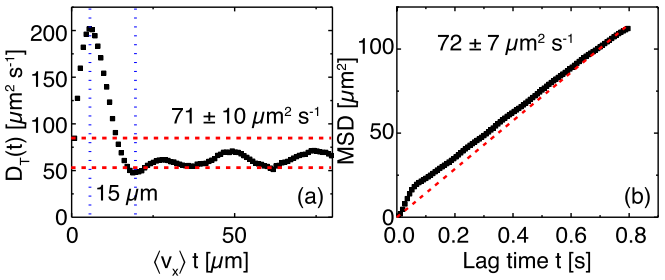

FIG. 9. Comparison of transverse dispersion coefficients obtained for 2-μm particles in HPAM solution in a square 45° array at a flow rate of 0.3 μl min^{-1}. (a) Extracted from the asymptotic value of the time-dependent dispersion coefficient $D_T(t)$ (shown here as a function of the distance traveled, $\langle v_x \rangle t$). (b) Extracted from the long-time slope of the mean-square displacement as a function of time.

of obstacles negligibly affected the increase in longitudinal dispersion, which was controlled by the extent of deformation or nonlinearity of the flow. The scaling of D_T/D_0, however, again depended on the geometry of the porous medium. In the ordered post arrays that were not aligned with the flow direction, the normalized transverse dispersion coefficients as a function of Wi could be fitted to

$$\frac{D_T}{D_0} = 1 + c(\mathrm{Wi} - \mathrm{Wi}_c)^{1.5\pm0.1}. \quad (4)$$

This fitting form, introduced in Ref. [3], captures the onset of elastic instabilities at Wi $\sim$ 1. Moreover, the fit exponent that describes the data in Fig. 7(d), $\alpha = 1.5 \pm 0.1$, was close to the value of $\alpha = 1.4$ obtained in Ref. [3] for experiments in a square 45° array. Our results in these geometries are therefore consistent with the idea, proposed in Ref. [3], that the enhanced dispersion is due to elastic instabilities that promote velocity fluctuations, and moreover that the periodic arrangement of the obstacles enhances these fluctuations [44]. In disordered media, however, whether the relatively sparse 2D random posts of these experiments [stars in Fig. 8(b)] or our earlier 3D dense packed-bed experiments (gray symbols in Fig. 8(b), Ref. [4]), D_T/D_0 depended only very weakly on Wi. This result suggests that enhanced transverse dispersion is not obtained when the transverse velocity fluctuations are averaged out by the structural disorder in the porous medium. Surprisingly, the behavior of transverse dispersion coefficients in the square 0° array was intermediate between these limits: these data did not collapse onto the master curve of the staggered ordered arrays, and exhibited a stronger dependence on Wi than the disordered media. We note that the nonlinear fluid response promoted streamline crossing, thereby allowing particles to enter the large stagnation zones and recirculating regions that often arise when shear-thinning fluids are flowed through porous media [54] and that indeed appeared between the posts when HPAM solutions were flowed through the square 0° array [cf. Fig. 2(m)]. We therefore suggest that the intermediate scaling of the transverse dispersion coefficients in this geometry reflected the competition between two effects: streamline crossing (which promoted transverse dispersion) and fluid recirculation (which, by locally trapping the particles, reduced large-scale transverse displacements).

IV. CONCLUSIONS

In this paper, we relate properties of the pore-scale trajectories of particles flowed through ordered or disordered 2D porous media to macroscale dispersion. The anisotropic stresses imparted by the deformation of the polymeric fluids flowed at high Wi enhanced the fluctuations in the velocity, which in turn promoted streamline crossing. Whether transverse dispersion was enhanced by these fluctuations, however, depended on the underlying geometric structure of the medium: whereas in an ordered medium the transverse fluctuations regularly compounded, in a disordered medium the fluctuations were averaged out by the structural disorder. This averaging-out occurred in both the relatively dilute 2D microfluidic post arrays presented here as well as in the 3D

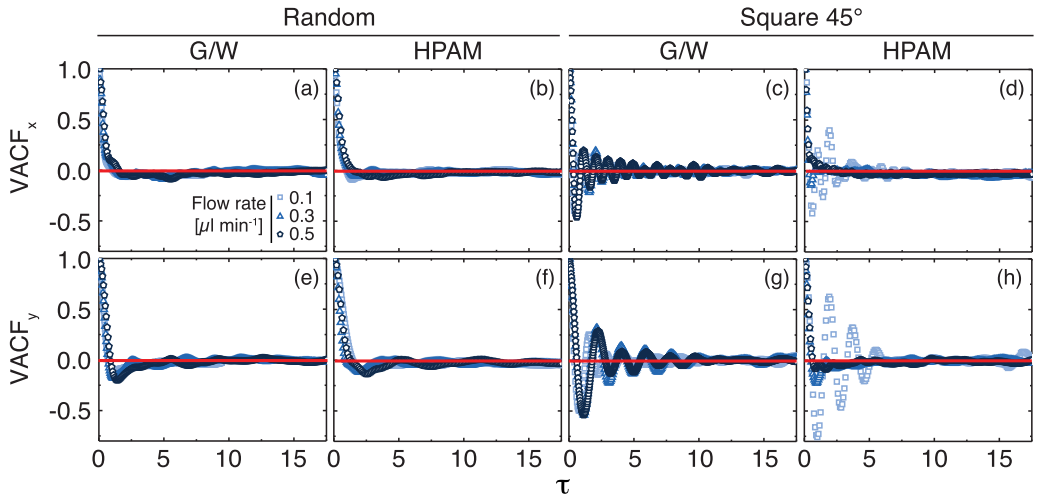

FIG. 10. Longitudinal (a–d) and transverse (e–h) velocity autocorrelation functions as a function of the normalized lag time $\tau = t\langle v_x \rangle / d_c$ of 2-μm particles in 90% glycerol-water (a, c, e, g) or 0.1% HPAM (b, d, f, h) solutions. The posts were randomly oriented (a, b, e, f) or arranged in a square lattice oriented 45° with respect to the incident flow (c, d, g, h). The red line indicates a VACF of zero. Symbols indicate flow rates: 0.1 μl min^{-1} (squares), 0.3 μl min^{-1} (triangles), 0.5 μl min^{-1} (pentagons).

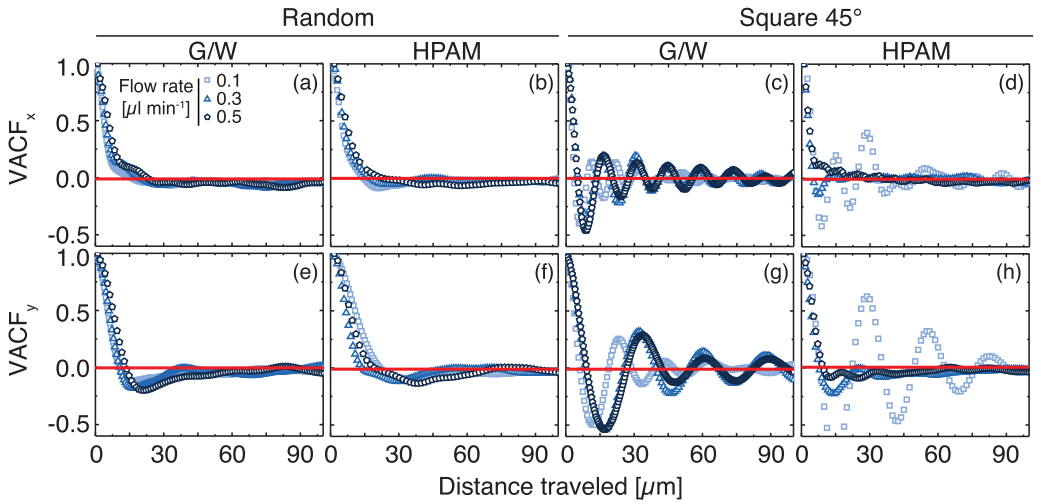

FIG. 11. Longitudinal (a–d) and transverse (e–h) velocity autocorrelation functions (VACFs) as a function of distance traveled, $\langle v_x \rangle t$, for 2-μm particles in 90% glycerol-water (a, c, e, g) or 0.1% HPAM (b, d, f, h) solutions. The posts were randomly oriented (a, b, e, f) or arranged in a square lattice oriented 45° with respect to the incident flow (c, d, g, h). The red line indicates a VACF of zero. Symbols indicate flow rates: 0.1 μl min^{-1} (squares), 0.3 μl min^{-1} (triangles), 0.5 μl min^{-1} (pentagons).

dense packed beds of Ref. [4]. Hence, this study suggests that coupling between the fluid deformation and the geometric structure of the medium controls the transverse dispersion of particles therein. By contrast, the longitudinal dispersion coefficients scaled linearly with both Pe (for both Newtonian glycerol-water and the shear-thinning polymer solution) and with Wi, independent of the geometry of the porous medium.

While our experiments suggest a simple interpretation for distinguishing the effects of dispersion based on structural order, predicting dispersion for particles flowed through

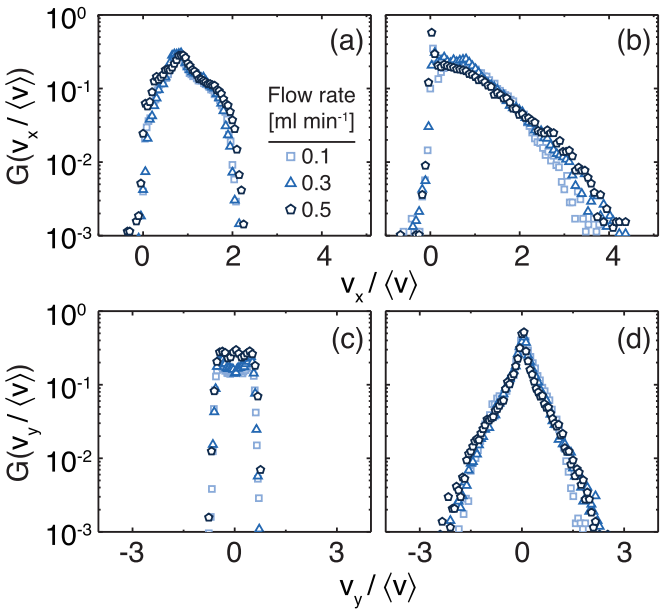

FIG. 12. Distributions of normalized longitudinal (x, top row) and transverse (y, bottom row) velocities of 2-μm particles in (a, c) 90% glycerol-water or (b, d) 0.1% HPAM solutions in a hexagonal post array. Symbols indicate flow rates: 0.1 μl min^{-1} (squares), 0.3 μl min^{-1} (triangles), 0.5 μl min^{-1} (pentagons).

porous media in applied settings may require additional physical considerations. First, the spherical particles used in these experiments ($d_p = 2\,\mu$m) were much smaller than the length scale characterizing the extent of confinement, the edge-to-edge spacing between the posts ($S = 15\,\mu$m), leading to a confinement ratio $d_p/S \approx 0.13$. This value is somewhat below the threshold required to observe deviations from the bulk transport properties in earlier 2D experiments [24]. As characteristic pore or throat sizes are decreased, the particles cannot be treated as infinitesimal tracers and hydrodynamic interactions with the posts may lead to deterministic streamline switching [21,22]. Moreover, in this limit the fluid is increasingly deformed and interactions between particles and nearby surfaces become increasingly important, but effects of strong confinement on dispersion in the presence of rheologically complex fluids remains to be explored. Second, the particles interacted neutrally or repulsively with the surfaces of the posts or packed beds. Attractive interactions may increase the residence time of particles near surfaces [5] or even lead to irreversible adsorption and clogging [74], but connecting features induced by attractions in the pore-scale trajectories to their effects on macroscopic dispersion has not been systematically undertaken. Similarly, particles that are anisotropic or inhomogeneous in shape, softness, or chemical functionality may interact very differently with distinct regions within the porous medium. Third, these experiments employ one prototypical non-Newtonian fluid, a shear-thinning polymer solution. How the confined rheological properties of other fluid models [40,41,75,76] alter the trajectories of particles within porous media remains to be investigated. These and similar studies that connect pore-scale trajectories to macroscale dispersion across a broad range of particle-matrix interactions and fluid rheological properties are expected to greatly improve the ability to predict particle transport for applications ranging from drug delivery to environmental remediation to nanocomposite processing.

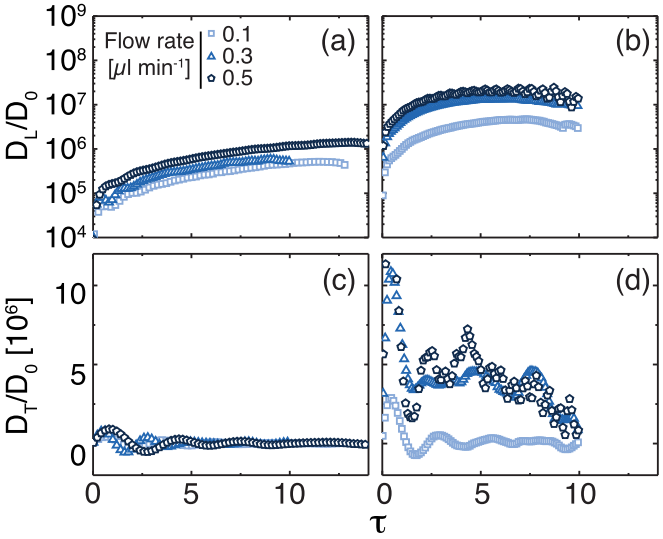

FIG. 13. Normalized longitudinal $[D_L(\tau)/D_0$ (a, b)] and transverse $[D_T(\tau)/D_0$ (c, d)] dispersion coefficients as a function of the normalized lag time $\tau = t\langle v_x\rangle/d_c$ for 2-μm particles in 90% glycerol-water (a, c) or 0.1% HPAM (b, d) solutions in a square 0° array. Symbols indicate flow rates: 0.1 μl min^{-1} (squares), 0.3 μl min^{-1} (triangles), 0.5 μl min^{-1} (pentagons).

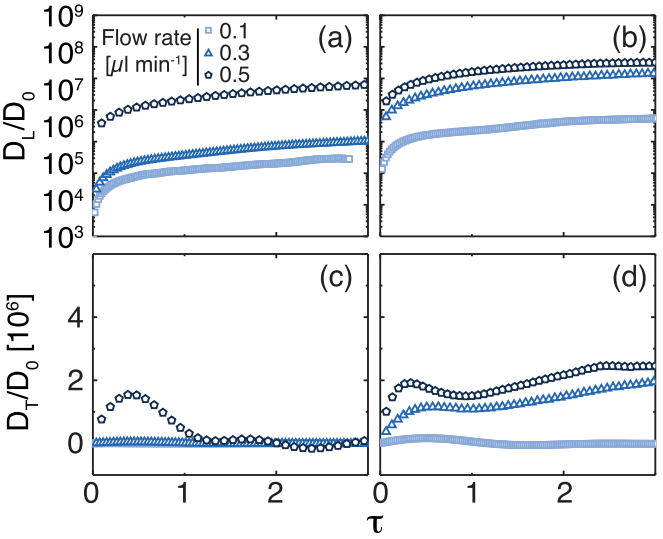

FIG. 14. Normalized longitudinal $[D_L(\tau)/D_0$ (a, b)] and transverse $[D_T(\tau)/D_0$ (c, d)] dispersion coefficients as a function of the normalized lag time $\tau = t\langle v_x\rangle/d_c$ for 2-μm particles in 90% glycerol-water (a, c) or 0.1% HPAM (b, d) solutions in a hexagonal array. Symbols indicate flow rates: 0.1 μl min^{-1} (squares), 0.3 μl min^{-1} (triangles), 0.5 μl min^{-1} (pentagons).

ACKNOWLEDGMENTS

We thank Debora F. Rodrigues for the use of the Leica SP8 microscope and Megan L. Robertson for use of the TA Hybrid Discovery rheometer. R.K. acknowledges funding from ExxonMobil Company. J.C.C. acknowledges funding from NSF (Grant No. CBET-1438204) and the Welch Foundation (Grant No. E-1869).

APPENDIX A: SUPPLEMENTAL TABLES

Table I contains the areal density and porosity of the posts. The latter was calculated as the area of the void space divided by the total area and represents the fraction of the array occupied by voids.

Tables II–IV contain the values of two dimensionless numbers calculated for different experiments. The Péclet number, the ratio of the rates of advection and diffusion, was calculated as $\mathrm{Pe} = \langle v_x\rangle d_p/D_0$, where $d_p = 2\,\mu$m is the particle diameter, $\langle v_x\rangle$ is the average longitudinal velocity, and D_0 is the diffusion coefficient measured in quiescent conditions. The Weissenberg number, the ratio of viscous and elastic forces, was calculated as $\mathrm{Wi} = \lambda\langle v_x\rangle/h$, where $\lambda = 15$ s is the polymer relaxation time and $h = 8\,\mu$m is the height of the channel.

APPENDIX B: SUPPLEMENTAL FIGURES

In this appendix we provide additional figures (Figs. 9–14) to justify statements made in the main text. Figure 9 shows that the different methods for extracting the transverse dispersion coefficients produce similar values of D_T. Figures 10 and 11 present representative velocity autocorrelation functions for particles in random and square 45° arrays as a function of the normalized lag time and distance traveled, respectively. Figure 12 presents the velocity distributions for particles in hexagonal arrays. Figures 13 and 14 present the time-dependent dispersion coefficients in square 0° and hexagonal arrays.

[1] V. Chaplain, C. Allain, and J. P. Hulin, Eur. Phys. J. B **6**, 225 (1998).

[2] J. A. Pathak, D. Ross, and K. B. Migler, Phys. Fluids **16**, 4028 (2004).

[3] C. Scholz, F. Wirner, J. R. Gomez-Solano, and C. Bechinger, Europhys. Lett. **107**, 054003 (2014).

[4] F. Babayekhorasani, D. E. Dunstan, R. Krishnamoorti, and J. C. Conrad, Soft Matter **12**, 5676 (2016).

[5] F. Babayekhorasani, D. E. Dunstan, R. Krishnamoorti, and J. C. Conrad, Soft Matter **12**, 8407 (2016).

[6] R. Ponnapati, O. Karazincir, E. Dao, R. Ng, K. K. Mohanty, and R. Krishnamoorti, Ind. Eng. Chem. Res. **50**, 13030 (2011).

[7] H. ShamsiJazeyi, C. A. Miller, M. S. Wong, J. M. Tour, and R. Verduzco, J. Appl. Polym. Sci. **131**, 40576 (2014).

[8] H. Zhang, A. Nikolov, and D. Wasan, Energy Fuels **28**, 3002 (2014).

[9] H. Ehtesabi, M. M. Ahadian, and V. Taghikhani, Energy Fuels **29**, 1 (2015).

[10] W. Tungittiplakorn, C. Cohen, and L. W. Lion, Environ. Sci. Technol. **39**, 1354 (2005).

[11] X. Zhao, W. Liu, Z. Cai, B. Han, T. Qian, and D. Zhao, Water Res. **100**, 245 (2016).

[12] R. Tang, C. S. Kim, D. J. Solfiell, S. Rana, R. Mout, E. M. Velázquez-Delgado, A. Chompoosor, Y. Jeong, B. Yan,

Z.-J. Zhu, C. Kim, J. A. Hardy, and V. M. Rotello, ACS Nano **7**, 6667 (2013).
[13] E. Vlashi, L. E. Kelderhouse, J. E. Sturgis, and P. S. Low, ACS Nano **7**, 8573 (2013).
[14] A. Parodi, S. G. Haddix, N. Taghipour, S. Scaria, F. Taraballi, A. Cevenini, I. K. Yazdi, C. Corbo, R. Palomba, S. Z. Khaled, J. O. Martinez, B. S. Brown, L. Isenhart, and E. Tasciotti, ACS Nano **8**, 9874 (2014).
[15] C. Zhang, D. Ni, Y. Liu, H. Yao, W. Bu, and J. Shi, Nat. Nanotechnol. **12**, 378 (2017).
[16] D. Koch and J. F. Brady, J. Fluid Mech. **154**, 399 (1985).
[17] U. M. Scheven, Phys. Rev. Lett. **110**, 214504 (2013).
[18] P. G. Saffman, J. Fluid Mech. **6**, 321 (1959).
[19] H. Brenner, Philos. Trans. R. Soc. London A **297**, 81 (1980).
[20] A. Daneyko, D. Hlushkou, S. Khirevich, and U. Tallarek, J. Chromatogr., A **1257**, 98 (2012).
[21] L. R. Huang, E. C. Cox, R. H. Austin, and J. C. Sturm, Science **304**, 987 (2004).
[22] J. Frechette and G. Drazer, J. Fluid Mech. **627**, 379 (2009).
[23] D. Hlushkou, S. Piatrusha, and U. Tallarek, Phys. Rev. E **95**, 063108 (2017).
[24] K. He, S. T. Retterer, B. R. Srijanto, J. C. Conrad, and R. Krishnamoorti, ACS Nano **8**, 4221 (2014).
[25] M. Auset and A. A. Keller, Water Resour. Res. **40**, W03503 (2004).
[26] R. C. Bales, C. P. Gerba, G. H. Grondin, and S. L. Jensen, Appl. Environ. Microbiol. **55**, 2061 (1989).
[27] H. Brenner, Chem. Eng. Sci. **16**, 242 (1961).
[28] K. He, F. Babaye Khorasani, S. T. Retterer, D. K. Thomas, J. C. Conrad, and R. Krishnamoorti, ACS Nano **7**, 5122 (2013).
[29] S. Sasidharan, S. Torkzaban, S. A. Bradford, P. J. Dillon, and P. G. Cook, Colloids Surf. A **457**, 169 (2014).
[30] J. D. C. Jacob, K. He, R. Krishnamoorti, and J. C. Conrad, Soft Matter **11**, 7515 (2015).
[31] H. F. Lecoanet, J.-Y. Bottero, and M. R. Wiesner, Environ. Sci. Technol. **38**, 5164 (2004).
[32] N. Tufenkji and M. Elimelech, Environ. Sci. Technol. **38**, 529 (2004).
[33] A. Tiraferri and R. Sethi, J. Nanopart. Res. **11**, 635 (2009).
[34] D. W. Meyer and B. Bijeljic, Phys. Rev. E **94**, 013107 (2016).
[35] F. Babaye Khorasani, R. Poling-Skutvik, R. Krishnamoorti, and J. C. Conrad, Macromolecules **47**, 5328 (2014).
[36] R. Poling-Skutvik, R. Krishnamoorti, and J. C. Conrad, ACS Macro Lett. **4**, 1169 (2015).
[37] R. Poling-Skutvik, K. I. S. Mongcopa, A. Faraone, S. Narayanan, J. C. Conrad, and R. Krishnamoorti, Macromolecules **49**, 6568 (2016).
[38] D. L. Dauben and D. E. Menzie, J. Petrol. Technol. **19**, 1065 (1967).
[39] T. Sochi, Polymer **51**, 5007 (2010).
[40] T. Chevalier, S. Rodts, X. Chateau, C. Chevalier, and P. Coussot, Phys. Rev. E **89**, 023002 (2014).
[41] S. Shahsavari and G. H. McKinley, J. Non-Newtonian Fluid Mech. **235**, 76 (2016).
[42] S. P. Sullivan, L. F. Gladden, and M. L. Johns, J. Non-Newtonian Fluid Mech. **133**, 91 (2006).
[43] S. Kenney, K. Poper, G. Chapagain, and G. F. Christopher, Rheol. Acta **52**, 485 (2013).
[44] X. D. Shi and G. F. Christopher, Phys. Fluids **28**, 124102 (2016).
[45] R. G. Larson, E. S. G. Shaqfeh, and S. J. Muller, J. Fluid Mech. **218**, 573 (1990).
[46] P. Pakdel and G. H. McKinley, Phys. Rev. Lett. **77**, 2459 (1996).
[47] J. Zilz, R. J. Poole, M. A. Alves, D. Bartolo, B. Levache, and A. Lindner, J. Fluid Mech. **712**, 203 (2012).
[48] M. Cromer, L. P. Cook, and G. H. McKinley, J. Non-Newtonian Fluid Mech. **166**, 566 (2011).
[49] T. Divoux, M. A. Fardin, S. Manneville, and S. Lerouge, Annu. Rev. Fluid Mech. **48**, 81 (2016).
[50] H. Bodiguel, J. Beaumont, A. Machado, L. Martinie, H. Kellay, and A. Colin, Phys. Rev. Lett. **114**, 028302 (2015).
[51] W. P. Cox and E. H. Merz, J. Polym. Sci. **28**, 619 (1958).
[52] J. C. Crocker and D. G. Grier, J. Colloid Interface Sci. **179**, 298 (1996).
[53] R. S. Maier, D. M. Kroll, R. S. Bernard, S. E. Howington, J. F. Peters, and H. T. Davis, Phys. Fluids **12**, 2065 (2000).
[54] D. Kawale, E. Marques, P. L. J. Zitha, M. T. Kreutzer, W. R. Rossen, and P. E. Boukany, Soft Matter **13**, 765 (2017).
[55] R. Haas and F. Durst, Viscoelastic flow of dilute polymer solutions in regularly packed beds, in *Progress and Trends in Rheology: Proceedings of the First Conference of European Rheologists Graz (Austria), April 14–16, 1982*, edited by H. Giesekus, K. Kirschke, and J. Schurz (Steinkopff, Heidelberg, 1982), pp. 212–217.
[56] A. Magueur, M. Moan, and G. Chauveteau, Chem. Eng. Commun. **36**, 351 (1985).
[57] F. Durst, R. Haas, and W. Interthal, J. Non-Newtonian Fluid Mech. **22**, 169 (1987).
[58] J. A. Odell and S. J. Haward, Rheol. Acta **47**, 129 (2008).
[59] A. Machado, H. Bodiguel, J. Beaumont, G. Clisson, and A. Colin, Biomicrofluidics **10**, 043507 (2016).
[60] M. Grilli, A. Vázquez-Quesada, and M. Ellero, Phys. Rev. Lett. **110**, 174501 (2013).
[61] C. Chmielewski and K. Jayaraman, J. Non-Newtonian Fluid Mech. **48**, 285 (1993).
[62] B. Khomami and L. D. Moreno, Rheol. Acta **36**, 367 (1997).
[63] P. J. Oliveira and A. I. P. Miranda, J. Non-Newtonian Fluid Mech. **127**, 51 (2005).
[64] S. P. Sullivan, A. J. Sederman, M. L. Johns, and L. F. Gladden, J. Non-Newtonian Fluid Mech. **143**, 59 (2007).
[65] A. Clarke, A. M. Howe, J. Mitchell, J. Staniland, and L. A. Hawkes, SPE J. **21**, 675 (2016).
[66] S. S. Datta, H. Chiang, T. S. Ramakrishnan, and D. A. Weitz, Phys. Rev. Lett. **111**, 064501 (2013).
[67] P. G. de Gennes, J. Chem. Phys. **60**, 5030 (1974).
[68] D. Kandhai, D. Hlushkou, A. G. Hoekstra, P. M. A. Sloot, H. Van As, and U. Tallarek, Phys. Rev. Lett. **88**, 234501 (2002).
[69] B. Bijeljic and M. Blunt, Water Resour. Res. **43** (2007).
[70] S. Stapf, K. J. Packer, R. G. Graham, J. F. Thovert, and P. M. Adler, Phys. Rev. E **58**, 6206 (1998).
[71] C. L. Hackert, J. L. Ellzey, O. A. Ezekoye, and M. J. Hall, Exp. Fluids **21**, 286 (1996).
[72] J. M. P. Q. Delgado, Chem. Eng. Res. Des. **85**, 1245 (2007).
[73] J. M. Dealy, Rheol. Bull. **79**, 14 (2010).
[74] Z. B. Sendekie and P. Bacchin, Langmuir **32**, 1478 (2016).
[75] J. Bleyer and P. Coussot, Phys. Rev. E **89**, 063018 (2014).
[76] E. J. Hemingway, A. Clarke, J. R. A. Pearson, and S. M. Fielding, arXiv:1701.04233 (2017).